# Photodissociation dynamics of $CH_2I_2$ molecules in the ultraviolet range studied by ion imaging

Haifeng Xu, Ying Guo, Shilin Liu, Xingxiao Ma, Dongxu Dai, and Guohe Sha

---

## Articles you may be interested in

Photofragmentation infrared emission studies of vibrationally excited free radicals $CH_3$ and $CH_2I$
The Journal of Chemical Physics **72**, 6531 (2008); 10.1063/1.439111

Velocity map imaging of ions and electrons using electrostatic lenses: Application in photoelectron and photofragment ion imaging of molecular oxygen
Review of Scientific Instruments **68**, 3477 (1998); 10.1063/1.1148310

Time-resolved multi-mass ion imaging: Femtosecond UV-VUV pump-probe spectroscopy with the PImMS camera
The Journal of Chemical Physics **147**, 013911 (2017); 10.1063/1.4978923

Tunneling effects in the unimolecular decay of $(CH_3)_2COO$ Criegee intermediates to OH radical products
The Journal of Chemical Physics **146**, 134307 (2017); 10.1063/1.4979297

The electronic state-selective photodissociation of $CH_2BrI$ at 248, 210, and 193 nm
The Journal of Chemical Physics **86**, 2051 (1998); 10.1063/1.452155

$CH_2I_2$ photodissociation: Dynamical modeling
The Journal of Chemical Physics **89**, 3602 (1998); 10.1063/1.454880

---

# Photodissociation dynamics of $CH_2I_2$ molecules in the ultraviolet range studied by ion imaging

Haifeng Xu, Ying Guo, Shilin Liu,[a] and Xingxiao Ma
*Open Laboratory of Bond Selective Chemistry, Department of Chemical Physics,*
*University of Science and Technology of China, Hefei, Anhui 230026, China*

Dongxu Dai and Guohe Sha
*State Key Laboratory of Molecular Reaction Dynamics, Dalian Institute of Chemical Physics,*
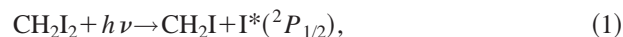*Chinese Academy of Science, Dalian 116023, China*

The photodissociation dynamics of diiodomethane molecules has been investigated in the wavelength range of 277–305 nm by an ion imaging spectrometer operated under optimal conditions for velocity mapping, where the ions were generated from $(2+1)$ multiphoton ionization of $I(^2P_{3/2})$ and $I^*(^2P_{1/2})$ fragments with the same laser as that to dissociate the parent molecules. The speed and angular distributions of $I^*$ and $I$ fragments were determined from the images. The translational energy distribution of $I^*(^2P_{1/2})$ fragment consists of a single Gaussian component (named $G^*$), while that of $I(^2P_{3/2})$ consists of two Gaussian components (named $G1$ and $G2$). It was found that the component $G^*$ and $G2$ show similar angular distributions and similar fragmentation energy partitioning ratios, indicating that these two components originate from dissociation at the same electronically excited state, while the component $G1$ is from another state. Three fragmentation pathways were employed to account for the experimental observations, the adiabatic dissociation from the $1B_1$ state to form $I(^2P_{3/2})$ with component $G1$, the adiabatic dissociation from the $2B_1$ state to form $I^*(^2P_{1/2})$ with component $G^*$, and the nonadiabatic dissociation from the $2B_1$ state caused by coupling with the higher $2A_1$ state to form $I(^2P_{3/2})$ with component $G2$. © *2002 American Institute of Physics.* [DOI: 10.1063/1.1503316]

## I. INTRODUCTION

Small polyatomic molecules have been of interest for studies of molecular spectroscopy and photodissociation dynamics for quite a long time. A lot of research work has been carried out on the photodissociation dynamics of mono-halide molecules, such as the $CH_3I$ molecule.[1–4] However, relatively fewer investigations have been made on the di-halide molecules,[5,6] mainly due to the fact that the two C–X (X=F, Cl, Br, and I) bonds in these molecules make the structure of the electronically excited states, and thus the spectra related to them, fairly complicated. Figure 1 shows the absorption spectrum of the smallest dihalide molecule, $CH_2I_2$, in the ultraviolet visible (UV) wavelength range.[7] In contrast to that of iodomethane, which shows just a single broad band at around 260 nm, the absorption spectrum of $CH_2I_2$ can be convoluted into four broad band with Gaussian profiles centered at 312, 288, 249, and 212 nm.[5–8] As proposed in Ref. 8, these four bands correspond to transitions from the electronic ground state $X\,^1A_1$ to at least five electronically excited states, which were assigned as $1B_1$, $2B_1$, $B_2$, $1A_1$, and $2A_1$ in order of increasing energy. The electronic structure of $CH_2I_2$ and its dissociation dynamics in the UV range have long been the subject of interest, and have remained unclear to some extent.[5–12]

There are three possible dissociation channels of $CH_2I_2$ in the UV region:[12]

$$CH_2I_2 + h\nu \rightarrow CH_2I + I^*(^2P_{1/2}), \tag{1}$$

$$\rightarrow CH_2I + I(^2P_{3/2}), \tag{2}$$

$$\rightarrow CH_2 + I_2. \tag{3}$$

The dominant dissociation process with UV excitation is the rupture of the C–I bonds, i.e., channel (1) and/or channel (2). Although channel (3) is energetically possible at wavelengths below 333 nm, Schmitt and Comes[13] found from their flash photolysis experiment that is at most a minor dissociation pathway. Further studies by Koffend and Leone[11] and Cain *et al.*[14] showed that the $I_2$ fragment could not be formed from two lowest excited states, $1B_1$ and $2B_1$, from symmetry considerations. Early works using photofragment spectroscopy of Kawasaki *et al.*[8] in the range of 265–304 nm and by Kroger *et al.*[12] at 266 nm, showed that the $CH_2I_2$ molecule dissociates rapidly in the UV region compared to its rotational period to form the $CH_2I$ radical and $I(^2P_{3/2})$ or $I^*(^2P_{1/2})$ atoms, and suggested that the $CH_2I$ fragment might be highly internally excited. Subsequently, the vibrational state distribution of $CH_2I$ was determined by Leone and co-workers[7,11,15] employing the infrared fluorescence method at photolysis wavelengths of 248 nm and 308 nm. The quantum yield of $I^*(^2P_{1/2})$ in the range of 247–367 nm was measured using optoacoustical[10] and infrared fluorescence[11,15] methods. It was concluded that the lowest electronic transition

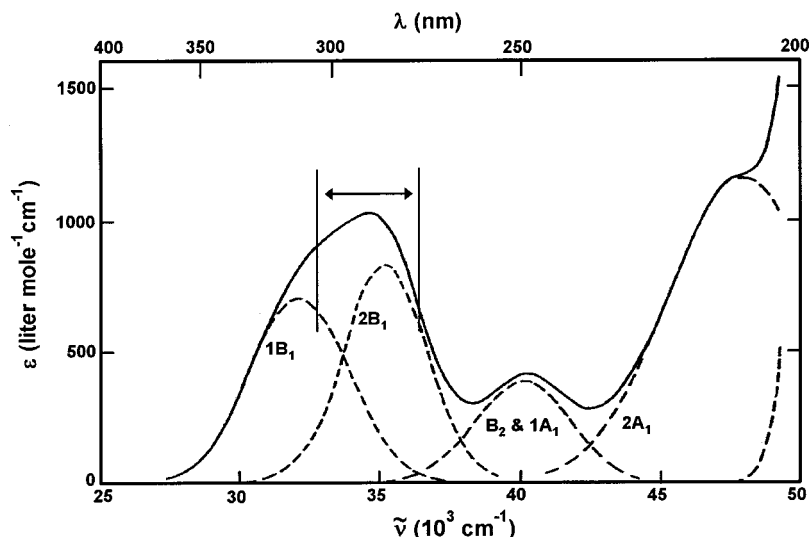[a]Author to whom correspondence should be addressed. Electronic mail: slliu@ustc.edu.cn

FIG. 1. Absorption spectrum of $CH_2I_2$ molecule in gas phase and its four deconvoluted Gaussian bands (dashed lines) in the range of 200–400 nm reported in Ref. 7. The assignments are taken from Ref. 8. The horizontal arrow indicates the photolysis wavelength range of 277–305 nm in the present study.

$(1B_1 \leftarrow X\,^1A_1)$ at $\lambda \sim 312$ nm yields only $I(^2P_{3/2})$ atoms, whereas the next higher transition $(2B_1 \leftarrow X\,^1A_1)$ at $\lambda \sim 288$ nm yields both $I^*(^2P_{1/2})$ and $I(^2P_{3/2})$ atoms. The nonunity quantum yield of $I^*(^2P_{1/2})$ at $\lambda \sim 288$ nm was interpreted by Koffend and Leone[11] with a possible curve-crossing mechanism between the initially excited $2B_1$ state and other electronic state(s). More recently, Jung et al.[16] studied the photofragment translational spectroscopy of $CH_2I_2$ at 304 nm by detecting $I^*(^2P_{1/2})$ and $I(^2P_{3/2})$ atoms with a linear time-of-flight (TOF) mass spectrometer, and obtained the fragmentation energy partitioning and the anisotropy parameters.

In this work, we used the ion velocity mapping technique to study the photodissociation dynamics of $CH_2I_2$ at several excitation wavelengths in the range of 277–305 nm. Such an experiment can measure the released translational energy distributions and the angular distributions of fragments with a relatively high resolution, and thus provide a deeper understanding of the dissociation mechanism in the UV region. Three different dissociation pathways, leading to different translational energy distributions and different fragmentation angular distributions for the products $I(^2P_{3/2})$ and $I^*(^2P_{1/2})$, were observed. Possible dissociation mechanisms were discussed based on the observations, and will be explained in detail in Sec. III. In Sec. II we describe the experiment briefly, and in Sec. IV we present our conclusions.

## II. EXPERIMENT

The basic experimental setup consists of a pulsed dye laser, a pulsed supersonic molecular beam, and a mass spectrometer operated under ion imaging conditions. Briefly, the gas mixture with 10% of $CH_2I_2$ (99.9% purity) seeded in argon gas at a total pressure of 760 torr was injected into a vacuum chamber through a pulsed valve (General Valve, $\phi 0.5$) and a skimmer. The supersonically cooled $CH_2I_2$ molecules were dissociated by a linearly polarized tunable UV laser, which was the frequency-doubled output of a dye laser (Lambda Physiks, LPD3002) pumped by a XeCl excimer laser (Lambda Physiks, LPX200). During the experiment, the polarization vector of the UV laser was set in a direction parallel to the detection axis. The atomic fragments, $I(^2P_{3/2})$ and $I^*(^2P_{1/2})$, were state-selectively ionized through a $(2+1)$ resonance enhanced multiphoton ionization process by focusing the same UV laser with a $f/500$ quartz lens. The generated ions were extracted and accelerated by specially designed electric fields, allowed to fly along the TOF tube with length of 30 cm, and finally were detected by a position-sensitive detector. The detector consists of a pair of microchannel plates (MCP) coupled to a fast phosphor screen. The fluorescence images from the phosphor screen were recorded by a cooled CCD camera ($768 \times 576$ pixel), and outputted to a personal computer for data acquisition.

The electric fields in our mass spectrometer were designed to operate the experiment under ion imaging conditions. The ion imaging technique, which was developed first by Parker et al.[17] in 1988, was improved in 1997 to allow ion velocity mapping.[18,19] During our experiment, the electric voltages of the extraction and acceleration fields were adjusted to reach optimal conditions for ion velocity focusing. A pulsed high electric voltage was applied to the MCP detector (mass gate) to selectively detect the desired ions and to ensure a maximum gain for the selected ions. The time delays between the pulsed value, the laser, the mass gate and the CCD camera were controlled by two pulse generators (SR, DG535).

The wavelengths of the UV laser used for both photodissociation and detection, were tuned to the two-photon resonant transitions of iodine atoms,[4] i.e., $5p\,^2P_{3/2} \rightarrow \rightarrow (^3P_0)6p[1]_{3/2}$ at $\lambda = 277.86$ nm, $5p\,^2P_{3/2} \rightarrow \rightarrow (^3P_2)6p[1]_{3/2}$ at $\lambda = 298.23$ nm, and $5p\,^2P_{3/2} \rightarrow \rightarrow (^3P_2)6p[1]_{1/2}$ at $\lambda = 303.69$ nm for the $I(^2P_{3/2})$ fragments; and $5p\,^2P_{1/2} \rightarrow \rightarrow (^1D_2)6p[1]_{1/2}$ at $\lambda = 277.40$ nm, $5p\,^2P_{1/2} \rightarrow \rightarrow (^1D_2)6p[3]_{5/2}$ at $\lambda = 281.73$ nm, and $5p\,^2P_{1/2} \rightarrow \rightarrow (^3P_1)6p[1]_{1/2}$ at $\lambda = 304.03$ nm for the $I^*(^2P_{1/2})$ fragments. During the experiment, the wavelength was scanned repeatedly over the whole Doppler linewidth to excite the fragments with different velocities. The intensity of the UV laser was maintained at 0.5 mJ/pulse to minimize the space charge effect between ionized fragments.

During the experiment, a small amount of $Na_2S_2O_3$ was

added to the liquid sample of $CH_2I_2$, which is the reservoir from which the $CH_2I_2$ vapor is generated, to eliminate the $I_2$ impurities contained. The static pressure in the photoionization region was about $3 \times 10^{-5}$ Pa, while the operating pressure during the experiment were about $2 \times 10^{-4}$ Pa.

## III. RESULTS AND DISCUSSION

### A. Translational energy distributions of fragments

Using the inverse Abel transform method, a full three-dimensional (3D) fragmentation image could be reconstructed from an observed two-dimensional (2D) image. Figure 2 displays the 3D images of the reconstructed recoil distributions of excited $I^*(^2P_{1/2})$ atoms resulting from photolysis of jet-cooled $CH_2I_2$ molecules at three different wavelengths as indicated in the images. Figure 3 shows the 3D images of ground $I(^2P_{3/2})$ atoms at another three different wavelengths. In both figures, the polarization vector of the photolysis laser is parallel to the vertical direction of the image plane. It can be seen clearly that all of the images have an angular distribution characteristic of a parallel transition, and that the recoil speed distribution of $I(^2P_{3/2})$ is much broader than that of $I^*(^2P_{1/2})$, indicating that the internal energy distribution of the $CH_2I$ fragment from the $I(^2P_{3/2})$ channel is much more broad than that from the $I^*(^2P_{1/2})$ channel. The images recorded at two pairs of wavelengths, 304.03 and 303.69 nm, and 277.40 and 277.86 nm, can be compared within each other to derive detailed information bout the fragmentation mechanism, since from the point of view of photodissociation the excitation energies at each of these two pairs of laser wavelengths are essentially the same.

By integrating the reconstructed 3D velocity distributions over all angles for each speed, the speed distributions of the two atomic fragments have been obtained, and have been converted to translational energy distributions, $P(E_t)$, which are related to the $CH_2I$ internal energy by energy conservation. The $P(E_t)$ distributions for $I^*(^2P_{1/2})$ and $I(^2P_{3/2})$ fragments obtained at the studied wavelengths are shown in Figs. 4 and 5, respectively. At each wavelength, the $P(E_t)$ distribution for $I^*(^2P_{1/2})$ is indeed much narrower than that for $I(^2P_{3/2})$. The former width at 304 nm is only about 500 cm$^{-1}$, while the latter width at 304 nm is about 1300 cm$^{-1}$. The broader $P(E_t)$ distribution for $I(^2P_{3/2})$ had been also observed by Jung *et al.*[16] in their study of fragment translational spectroscopy. However, due to the low resolution in translational energy using a normal TOF mass spectrometer, the structures in the $P(E_t)$ distribution could not be resolved. As can be seen clearly from Figs. 4 and 5, the $P(E_t)$ distributions obtained in this experiment consist of more than two components. These $P(E_t)$ distributions have been deconvoluted satisfactorily with several Gaussian functions, and the deconvoluted results are showed in the figures with dashed lines. The $P(E_t)$ distributions of $I^*(^2P_{1/2})$ consist of two components, a strong Gaussian component centered at about 1000 cm$^{-1}$, and a quite weak component with low translational energy. This strong component is named as component $G^*$ for convenience in the following discussion. In contrast, the $P(E_t)$ distributions of $I(^2P_{3/2})$ consist of four components, two strong components centered, respectively,
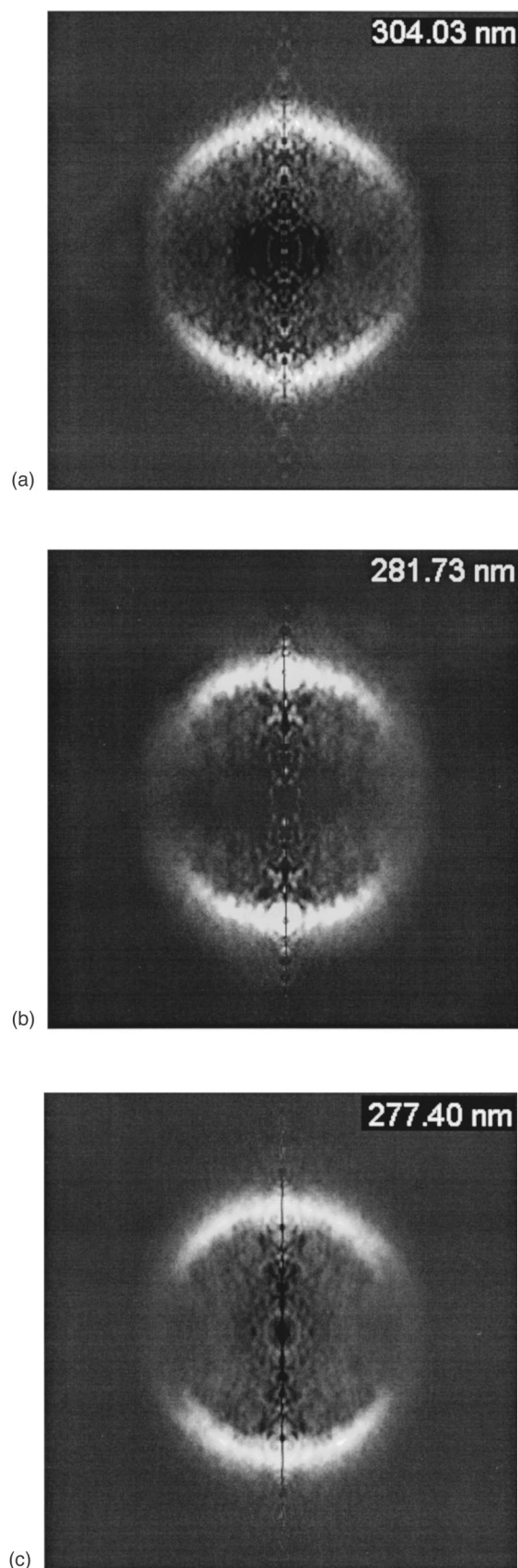


FIG. 2. Inverse Abel transformed ion velocity mapping of $I^*(^2P_{1/2})$ fragment formed in the photodissociation of $CH_2I_2$ at (a) 304.03 nm, (b) 281.73 nm, and (c) 277.40 nm. The electric field vector of the photolysis laser is parallel to the vertical direction of the image plane.
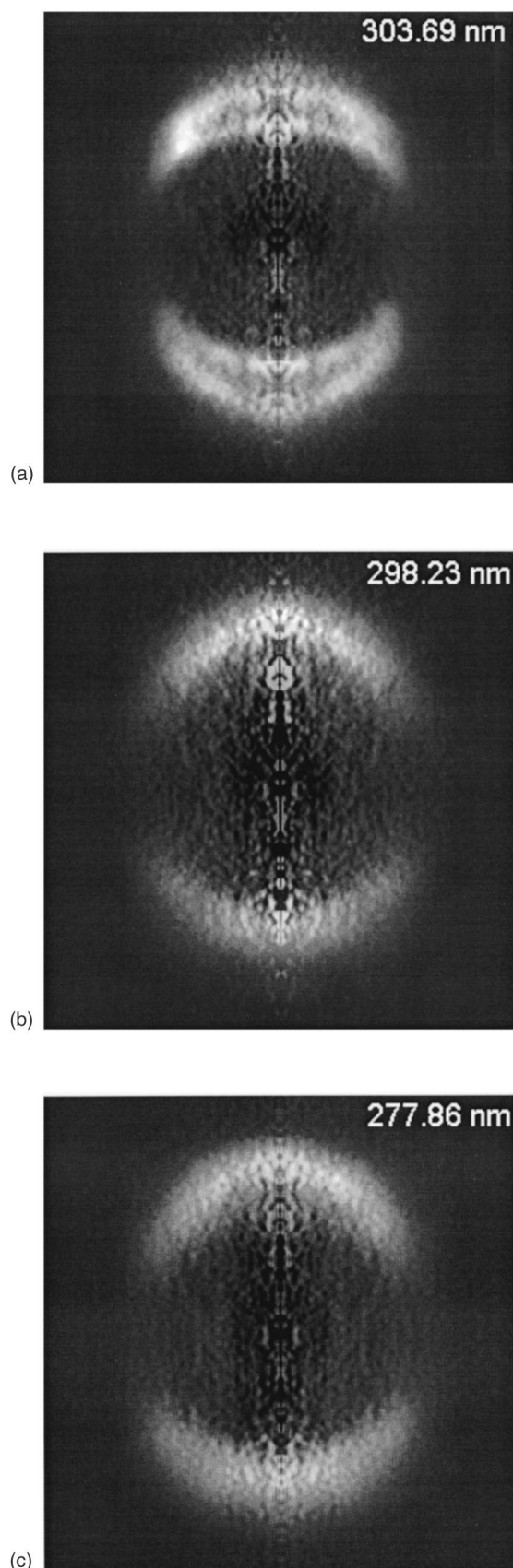
(a)

(b)

(c)

FIG. 3. Inverse Abel transformed ion velocity mapping of I($^2P_{3/2}$) fragment formed in the photodissociation of CH₂I₂ at (a) 303.69 nm, (b) 298.23 nm, and (c) 277.86 nm. The electric field vector of the photolysis laser is parallel to the vertical direction of the image plane.
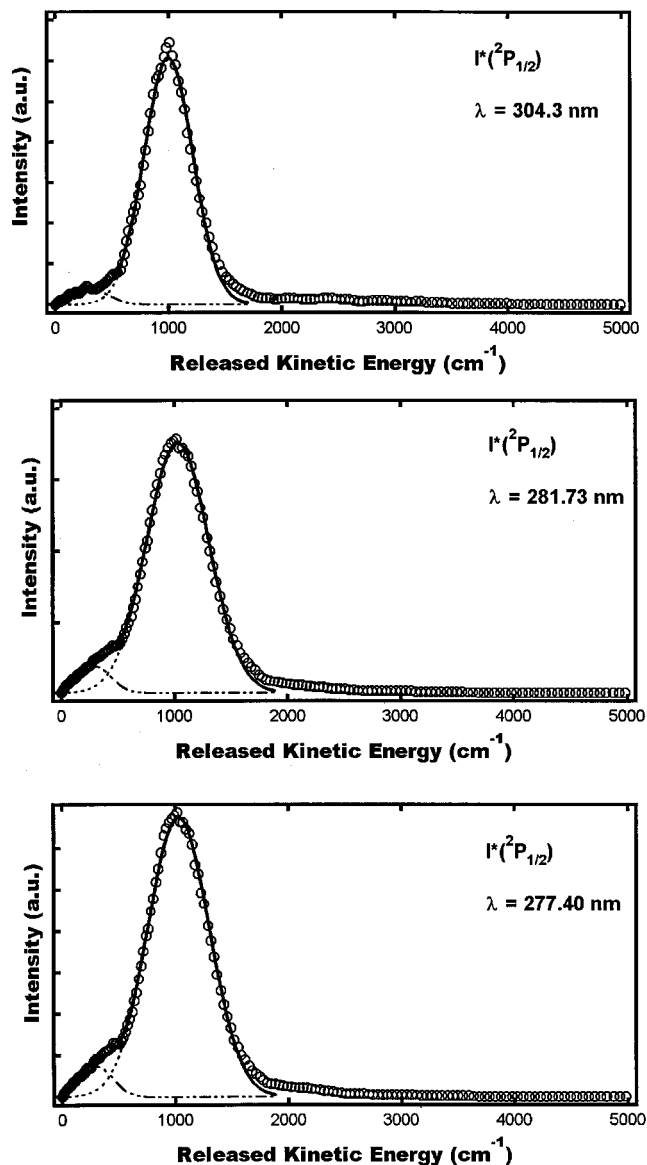


FIG. 4. Translational energy distributions for I*($^2P_{1/2}$) fragment from the photodissociation of CH₂I₂ determined from the measured ion images at the indicated photolysis wavelength. In each graph, the circle presents the experimental data, and the solid line represents the fitted result in terms of two Gaussian functions (dashed lines) which are centered, respectively, at ~300 and ~1000 cm$^{-1}$ (component $G^*$).

at about 1000 and 1900 cm$^{-1}$, and two weak components centered, respectively, at the lower and higher energy sides. The two main $P(E_t)$ components of I($^2P_{3/2}$) at 1000 and 1900 cm$^{-1}$ are named as components $G1$ and $G2$, respectively. In the following part, the three components, $G^*$, $G1$, and $G2$, will be our main concern to obtain information about the photodissociation mechanism of CH₂I₂ molecules, and the other weak components will be discussed in the final part of Sec. III C.

The remarkable difference between the $P(E_t)$ distributions of I*($^2P_{1/2}$) and I($^2P_{3/2}$) strongly suggests that the dissociation pathways of CH₂I₂ leading to these two fragments must be different. It seems that the I*($^2P_{1/2}$) fragment is mainly produced from one dissociation channel (for component $G^*$), while the I($^2P_{3/2}$) fragment is manly produced
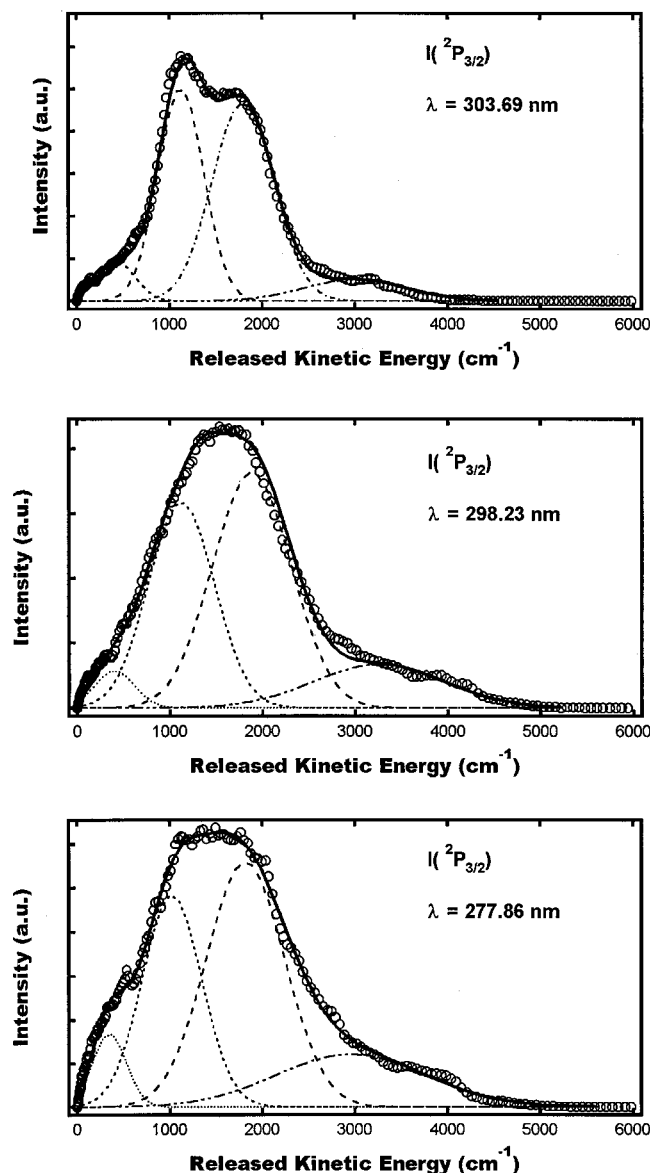
FIG. 5. Translational energy distributions for $I(^2P_{3/2})$ fragment from the photodissociation of $CH_2I_2$ determined from the measured ion images at the indicated photolysis wavelengths. In each graph, the circle presents the experimental data, and the solid line represents the fitted result in terms of four Gaussian functions (dashed lines) which are centered, respectively, at ~300 cm$^{-1}$, ~1000 cm$^{-1}$ (component $G1$), ~1900 cm$^{-1}$ (component $G2$), and ~3300 cm$^{-1}$ (component $G3$).

from two different channels (for components $G1$ and $G2$). A detailed analysis based on the energy partitionings and the angular distributions related to the three main components will be helpful to identify the dissociation mechanism of $CH_2I_2$ molecule.

The partitionings of excess energy into the translational and internal degrees of freedom of the fragments after dissociation were obtained by conservations of energy and momentum. For the dissociation channel (2) to form $I(^2P_{3/2})$ and $CH_2I$ fragments, the total available energy, $E_{avl}$, can be expressed as

$$E_{avl} = h\nu - D_0 = E_T + E_{int}, \qquad (4)$$

where $h\nu$ is the excitation photon energy, $D_0$ the dissociation

TABLE I. Partitioning of the available energy and anisotropy parameters in the dissociation of $CH_2I_2$ to form $I^*(^2P_{1/2})$ with $P(E_t)$ distribution component $G^*$ and $I(^2P_{3/2})$ with components $G1$ and $G2$ at different photolysis wavelengths. All the energies in the table are given in unit of cm$^{-1}$.

| Wavelength (nm) | Component | $E_{avl.}$ | $\langle E_T\rangle$ | $\langle E_{int}\rangle$ | $\langle E_{int}\rangle/E_{avl.}$ | $\beta$ |
|---|---|---|---|---|---|---|
| 277.40 | $I^*$, $G^*$ | 10 730 | 1900 | 8830 | 82% | 1.27(6) |
| 277.86 | I, $G1$ | 18 260 | 2000 | 16 260 | 89% | 1.05(6) |
|  | I, $G2$ |  | 3420 | 14 840 | 81% | 1.30(5) |
| 281.73 | $I^*$, $G^*$ | 10 170 | 2000 | 8170 | 80% | 1.32(5) |
| 298.23 | I, $G1$ | 15 800 | 2000 | 13 800 | 87% | 0.95(7) |
|  | I, $G2$ |  | 3900 | 11 900 | 75% | 1.24(6) |
| 303.69 | I, $G1$ | 15 200 | 2000 | 13 200 | 87% | 1.10(5) |
|  | I, $G2$ |  | 3610 | 11 590 | 76% | 1.31(5) |
| 304.03 | $I^*$, $G^*$ | 7570 | 1900 | 5670 | 75% | 1.33(6) |

energy of about 17 730 cm$^{-1}$,[7] $E_{int}$ the internal energy of $CH_2I$ fragment, and $E_T$ the total translational energy of $CH_2I$ and $I(^2P_{3/2})$ fragments obtained from the translational energy of $I(^2P_{3/2})$ based on momentum conservation. For the dissociation channel (1) to form $I^*(^2P_{1/2})$ and $CH_2I$ fragments, $h\nu - D_0$ should be subtracted by the spin–orbit splitting energy of iodine atom with the value of 7590 cm$^{-1}$ to yield $E_{avl}$. The values obtained for the most probable translational and internal energies, $\langle E_T\rangle$ and $\langle E_{int}\rangle$, at all studied wavelengths for the $P(E_t)$ distribution components, $G^*$, $G1$, and $G2$, are summarized in Table I. It can be seen that the $CH_2I$ fragment is produced with high internal excitation, and that the energy partition ratios, $\langle E_{int}\rangle/E_{avl}$, are on average about 80% at all the wavelengths studied. These observations are generally in good agreement with previous studies,[12,16] and could be predicted reasonably using an impulsive model for dissociation along a steep repulsive potential surface.[20]

It is interesting to notice that the $\langle E_{int}\rangle/E_{avl}$ ratios of the two $P(E_t)$ components of $I(^2P_{3/2})$ behave different. At both 277 nm and 304 nm, the $\langle E_{int}\rangle/E_{avl}$ ratios for component $G2$ of $I(^2P_{3/2})$ are quite closer to those for component $G^*$ of $I^*(^2P_{1/2})$, while those for component $G1$ have relatively larger values. This difference suggests that the $I(^2P_{3/2})$ fragment with component $G2$ may be produced from the same dissociation origin as the $I^*(^2P_{1/2})$ fragment, while the $I(^2P_{3/2})$ fragment with component $G1$ may be generated from another pathway. This assumption was confirmed further by the following analysis of angular distributions for these three $P(E_t)$ components.

## B. Fragmentation angular distributions

The fragmentation angular distribution $P(\theta,v)$ for a certain speed $v$ could be obtained by collecting data from the points with speed $v$ at each angle in the reconstructed 3D velocity distribution, where $\theta$ is the angle between the laser polarization direction and the recoil velocity of the photofragment. It was found that there is no significant difference of the $P(\theta,v)$ distributions within each of the $P(E_t)$ components, i.e., the fragments with various speeds in a single $P(E_t)$ component have the same angular distribution. Figure 6 shows the angular distributions of $I^*(^2P_{1/2})$ and $I(^2P_{3/2})$ at
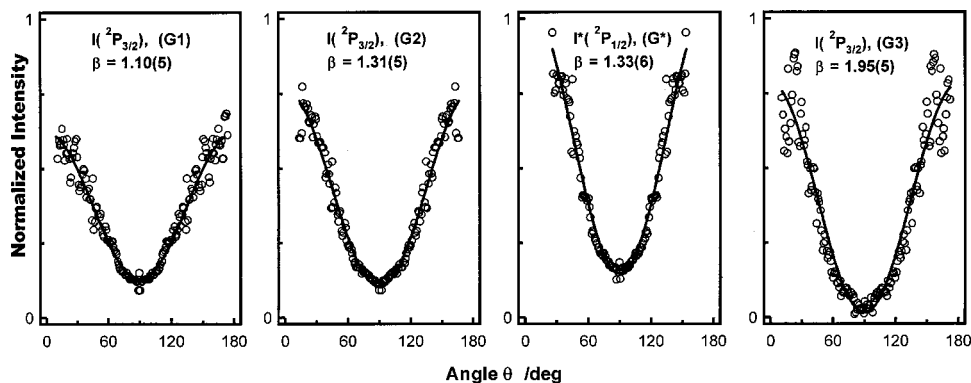
FIG. 6. Fragmentation angular distributions and the corresponding anisotropy parameters for I*($^2P_{1/2}$) with speed fixed at the peak position of component $G^*$ at $\lambda=304.03$ nm, and for I($^2P_{3/2}$) with speeds fixed at the peak positions of components $G1$, $G2$, and $G3$ at $\lambda=303.69$ nm. All distributions are normalized to unity area. The best fits according to Eq. (5) are represented by solid lines.

$\lambda\sim304$ nm for speeds at the peak positions of the components $G^*$, $G1$, and $G2$, represented, respectively, by $(G^*)$, $(G1)$, and $(G2)$ in the figure. Since the $P(E_t)$ components do not overlap seriously with each other at their peak positions as seen from Figs. 4 and 5, the curves in Fig. 6 can be viewed as representatives of the angular distributions of the whole corresponding $P(E_t)$ components.

In order to estimate an anisotropy parameter $\beta$, the angular distribution $P(\theta)$ has been fitted into the standard formula,[21]

$$P(\theta)\propto 1+\beta P_2(\cos(\theta)), \tag{5}$$

where $P_2(\cos(\theta))$ is the second-order Legendre polynomial. The best-fitted $P(\theta)$ curves are shown in Fig. 6 with solid lines, and the obtained $\beta$ values are indicated in the corresponding curves. The $\beta$ values at all the studied wavelengths for the three $P(E_t)$ components are listed in Table I.

Anisotropy parameter is important in describing the photodissociation dynamics, its limiting values for linear molecules are $+2$ or $-1$ for the electronic transition dipole moment $\mu$ parallel or perpendicular to the fragment recoil velocity $V$. As Kawasaki et al.[8] pointed out, CH$_2$I$_2$ can be treated as a triatomic molecule with $C_{2v}$ symmetry, and therefore the transition dipole moment lies parallel to the I–I direction for $B_1\leftarrow X\,^1A_1$ electronic transition, perpendicular to the I–C–I plane for $B_2\leftarrow X\,^1A_1$ transition, and at the bisecting direction of the I–C–I angle for $A_1\leftarrow X\,^1A_1$ transition. Assuming the I–C–I angle at electronically excited states to be 113° as in Ref. 8, the angle $\alpha$ between $\mu$ and $V$ in each case should be 33.5°, 90°, and 56.5°, respectively. Neglecting the lifetime of the electronically excited states, the $\beta$ values, given by $\beta\approx2P_2(\cos(\alpha))$,[20] for electronic transitions $B_1\leftarrow X\,^1A_1$, $B_2\leftarrow X\,^1A_1$, and $A_1\leftarrow X\,^1A_1$ should be 1.08, $-1$, and $-0.08$, respectively. Since the $\beta$ parameters obtained in this study have positive and around unity values for all three $P(E_t)$ components, the sign and magnitude of $\beta$ indicate that the dissociation of CH$_2$I$_2$ molecule should involve $B_1$ electronic state(s), and the dissociation rate of this state(s) should be very rapid compared to the rotational period of the CH$_2$I$_2$ molecule. These speculations were also suggested by previous studies.[5–8,12]

In early photofragment angular distribution studies of CH$_2$I$_2$, Kawasaki et al.[8] and Kroger et al.[12] reported, respectively, at 310 nm and 266 nm the $\beta$ values of 0.9 for overall I*($^2P_{1/2}$) and I($^2P_{3/2}$) fragments, while Jung et al.[16] reported

$\beta$ values of 0.55 for I*($^2P_{1/2}$) and 0.4 for I($^2P_{3/2}$) at 304 nm. Our obtained $\beta$ values are relatively larger than previous results. The difference may be due to the high resolution of the translational energies of I*($^2P_{1/2}$) and I($^2P_{3/2}$) in this experiment. The high resolution of the ion velocity mapping technique resolved the previously unobserved structures of the $P(E_t)$ distributions. The $\beta$ values in this experiment were obtained only for the main $P(E_t)$ components, i.e., components $G^*$, $G1$, and $G2$. As will be stated in the final part of Sec. III C, since the other components of the $P(E_t)$ distributions of I*($^2P_{1/2}$) and I($^2P_{3/2}$) on the low energy sides (inner parts of the 3D images) are less anisotropic, their contributions will decrease the $\beta$ values determined for the whole $P(E_t)$ distributions.

As seen from Table I, the interesting result we found is that at both 304 nm and 277 nm, the corresponding $\beta$ values of I($^2P_{3/2}$) for component $G2$ are close to those of I*($^2P_{1/2}$), but are different from those for the slower component $G1$. Recalling the values of energy partition ratios for the three $P(E_t)$ components as discussed in Sec. III A, the behavior, that the components $G2$ and $G^*$ are characterized by similar anisotropy parameter and energy partition ratio at each photolysis wavelength, confirms that the two channels producing the I($^2P_{3/2}$) fragment with component $G2$ and I*($^2P_{1/2}$) fragment start from the same electronic state of CH$_2$I$_2$, while the dissociation pathway producing I($^2P_{3/2}$) fragment with component $G1$ starts from a different electronic state, because of its different anisotropy parameters and energy partition ratios.

## C. Dissociation mechanism

The absorption spectrum of CH$_2$I$_2$ in the energy region below 50 000 cm$^{-1}$ is shown in Fig. 1.[7] The arrow represents the excitation energy region in this study. The three broad features in the spectrum have been deconvoluted into four bands centered at 312, 288, 249, and 212 nm.[7] A simple molecular calculation by Kawasaki et al.[8] suggested that at least five electronically excited states be involved in the four bands which were assigned as $1B_1$, $2B_1$, $B_2$, $1A_1$, and $2A_1$ in order of increasing energy, and that the $B_2$ and $1A_1$ states might be unresolved in the 249 nm band. The symmetry considerations[8,10,11,13,16] indicated that the $1B_1$ and $2A_1$ states correlate with the I($^2P_{3/2}$) dissociation limit, while the $2B_1$, $B_2$, and $1A_1$ states correlate with the I*($^2P_{1/2}$) disso-

ciation limit. Hunter *et al.*[10] and Koffend *et al.*[11] have measured the relative yield of I*($^2P_{1/2}$) atoms as a function of photolysis wavelength. They concluded that the lowest electronic transition to the $1B_1$ state at ~312 nm yields I($^2P_{3/2}$) atoms only, whereas the next higher transition to the $2B_1$ state at ~288 nm yields both I($^2P_{3/2}$) and I*($^2P_{1/2}$) atoms, probably due to a curve-crossing mechanism between the $2B_1$ state and other state(s).

In the present study, both $1B_1$ and $2B_1$ electronic states were excited due to the overlapping absorption in the excitation wavelength region, while the states with higher energies were excited very weakly. Therefore, it can be concluded that the I($^2P_{3/2}$) atom with either $P(E_t)$ component $G1$ or $G2$, is the result of adiabatic dissociation at the $1B_1$ electronic state, while the I*($^2P_{1/2}$) atom with component $G*$ is produced from adiabatic dissociation at the $2B_1$ electronic state. As concluded from the analyses of fragmentation energy partitionings and angular distributions, I($^2P_{3/2}$) atom with $P(E_t)$ component $G2$ is produced from the same dissociation origin as the I*($^2P_{1/2}$) atom, and it should be the result of indirect dissociation from the $2B_1$ electronic state. Therefore, totally three fragmentation pathways exist in the present excitation energy region, i.e., adiabatic dissociation from the $1B_1$ state to form I($^2P_{3/2}$) with component $G1$, adiabatic dissociation from the $2B_1$ state to form I*($^2P_{1/2}$) with component $G*$, and nonadiabatic dissociation from the $2B_1$ state caused by curve crossing with other electronic state(s) of $CH_2I_2$ to form I($^2P_{3/2}$) with component $G2$.

The relative variation of the I($^2P_{3/2}$) intensities of components $G1$ and $G2$ with excitation energy also confirms the above dissociation mechanism. It can be seen from Fig. 5 that the I($^2P_{3/2}$) intensity of component $G1$, compared with that of component $G2$, decreases with the excitation wavelength. According to the dissociation mechanism discussed above, the I($^2P_{3/2}$) fragment with component $G1$ is the direct dissociation product form the $1B_1$ state. Since the absorption of the $1B_1$ state becomes weaker as the wavelength decreases, the excitation efficiency to the $1B_1$ state and thus the intensity of component $G1$ decreases.

Curve crossing is a common phenomenon in molecular photodissociation process. In recent studies of other alkyl halides, such as $CH_2BrCl$ and $CBrCl_3$ molecules,[22,23] curve crossings were also observed. Figure 7 shows the schematic correlation energy diagram of $CH_2I_2$ molecules based on Refs. 8, 10, and 11 to illustrate the excitation–dissociation process. The block in the figure represents the excitation energy region in the present study. In this energy region, only $1B_1$ and $2B_1$ states could be excited. The adiabatic dissociation products from the $1B_1$ and $2B_1$ states are I($^2P_{3/2}$) and I*($^2P_{1/2}$) atoms, respectively. As the high $2A_1$ state correlates with the I($^2P_{3/2}$) dissociation limit, the nonadiabatic dissociation from the $2B_1$ electronic state, leading to I($^2P_{3/2}$) atom with $P(E_t)$ component $G2$, should be the result of curve crossing between the $2B_1$ and $2A_1$ electronic states. Since these two states are energetically far away from each other, the curve crossing must occur at a region far from the Franck–Condon excitation zone, i.e., near the exit of the adiabatic dissociation path of the $2B_1$ state. From a wave packet point of view, the initial wave packet created on the
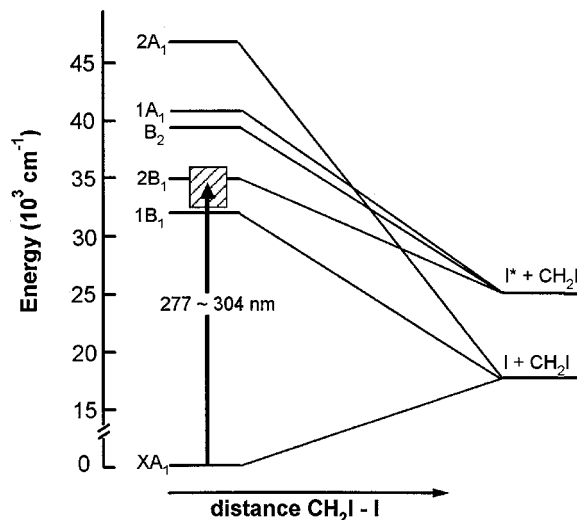


FIG. 7. Schematic energy diagram of the low-lying electronic states of $CH_2I_2$ correlating to the I*($^2P_{1/2}$) and I($^2P_{3/2}$) products based on Refs. 8, 10, and 11 to illustrate the adiabatic and nonadiabatic dissociation pathways. The block represents the excitation energy region studied in this experiment.

potential energy surface (PES) of the $2B_1$ state passes first along the dissociation path at short bond distance, and then separates into two parts at the curve crossing region. It continues to move on the PES of the $2B_1$ state, and finally leads to the I*($^2P_{1/2}$) atom with component $G*$; the other moves on the PES of the $2A_1$ state, leading to the I($^2P_{3/2}$) atom with component $G2$. Since the wave packet separates at the place close to the final stage of dissociation, the angular distribution and energy partitioning of component $G2$ should be similar to those of component $G*$. These are what we have observed in the experiment.

Besides the three main $P(E_t)$ distribution components discussed above, there still exists three weak $P(E_t)$ components to be discussed. The components, centered at 300–400 cm$^{-1}$ in each $P(E_t)$ distribution of I*($^2P_{1/2}$) and I($^2P_{3/2}$) fragments in Figs. 4 and 5, correspond to the inner parts of the 3D images in Figs. 2 and 3. It can be seen from the images that these components are less anisotropic. By checking with the results of the $CH_3I$ molecule at 277 nm, these components were confirmed to be real, and not to be experimental artifacts. We are not clear about the origins for these components. Because of the low translational energies and low anisotropy parameters for the components of the I($^2P_{3/2}$) fragments, a possible explanation is that they are probably produced by dissociation from the electronic ground state of the $CH_2I_2$ molecule after internal conversion from the electronically excited state to the high vibrational levels of the electronic ground state. The third component centered at about 3000 cm$^{-1}$ in the $P(E_t)$ distribution of the I($^2P_{3/2}$) fragment in Fig. 5 (named as component $G3$) is much broader than the others. As shown in Fig. 6, its corresponding $\beta$ value at 303.69 nm was determined to be 1.95 which is very close to the limiting value of +2 for linear molecules, indicating that the electronic transition associated to this component is parallel. A two-step dissociation mechanism proposed by Kroger *et al.*[12] at 266 nm may be a possible explanation. That is, the $CH_2I$ fragment after formation ab-

sorbs a second photon to form CH$_2$ and I($^2P_{3/2}$) fragments. Therefore, the initial translational and internal energy distributions of the CH$_2$I radical will broaden the translational energy distribution of the I($^2P_{3/2}$) atom from the CH$_2$I dissociation. Since the CH$_2$I radical can be treated as a pseudodiatomic molecule, and the electronic transition dipole moment from ground state is parallel to the CH$_2$–I bond, the related $\beta$ parameter should have a limit value of $+2$.

## IV. SUMMARY

In the present work, the photodissociation dynamics of CH$_2$I$_2$ at several wavelengths in the range of 277–305 nm has been studied with the ion velocity mapping technique. The translational energy distributions of the I*($^2P_{1/2}$) fragment are mainly described by one Gaussian function at all wavelengths (component $G^*$), while those of the I($^2P_{3/2}$) fragment are mainly described by two Gaussian functions (components $G1$ and $G2$). The $G^*$ and $G2$ components show similar fragmentation energy partition ratios and similar fragment angular distributions which are different from those of component $G1$, indicating that the I*($^2P_{1/2}$) fragment and I($^2P_{3/2}$) fragment with component $G2$ are generated from the same initial electronic state, while I($^2P_{3/2}$) fragment with component $G1$ is generated from another electronic state. With the aid of the previous studies, it is suggested that the I*($^2P_{1/2}$) atom and I($^2P_{3/2}$) atom with component $G2$ are, respectively, results of direct dissociation from the $1B_1$ and $2B_1$ electronic states of CH$_2$I$_2$, while the I($^2P_{3/2}$) atom with component $G1$ is generated from the indirect dissociation from the $2B_1$ state caused by curve crossing with higher $2A_1$ state.

[1] S. J. Riley and K. R. Wilson, Discuss. Faraday Soc. **53**, 132 (1972).
[2] Y. Jiang, M. R. Giorgi-Arnazzi, and R. B Berstein, Chem. Phys. **106**, 171 (1986).
[3] D. M. Szatlarski, R. van der Berg, and M. A. ElSayed, J. Phys. Chem. **93**, 6700 (1989).
[4] Y. J. Jung, Y. S. Kim, W. K. Kang, and K. H. Jung, J. Chem. Phys. **107**, 7187 (1997).
[5] W. M. Kwok and D. L. Phillips, J. Chem. Phys. **104**, 2529 (1996).
[6] J. Zhang and D. G. Imre, J. Chem. Phys. **89**, 309 (1988).
[7] S. L. Baughcum and S. R. Leone, J. Chem. Phys. **72**, 6531 (1980).
[8] M. Kawasaki, S. J. Lee, and R. Bersohn, J. Chem. Phys. **63**, 809 (1975).
[9] J. Zhang, E. J. Heller, D. Huber, D. G. Imre, and D. Tannor, J. Chem. Phys. **89**, 3602 (1988).
[10] T. F. Hunter and K. S. Kristjansson, Chem. Phys. Lett. **90**, 35 (1982).
[11] J. B. Koffend and S. R. Leone, Chem. Phys. Lett. **81**, 136 (1981).
[12] P. M. Kroger, P. C. Demou, and S. J. Riley, J. Chem. Phys. **65**, 1823 (1976).
[13] G. Schmitt and F. J. Comes, J. Photochem. **14**, 107 (1980).
[14] S. R. Cain, R. Hoffmann, and R. Grant, J. Phys. Chem. **85**, 4046 (1981).
[15] S. L. Baughcum, H. Hofmann, S. R. Leone, and D. J. Nesbitt, Faraday Discuss. Chem. Soc. **67**, 306 (1979).
[16] K. W. Jung , T. S. Ahmadi, and M. A. ElSayed, Bull. Korean Chem. Soc. **18**, 1274 (1997).
[17] J. W. Thoman, Jr., D. W. Chandler, D. H. Parker, and M. H. M. Janssea, Laser Chem. **9**, 27 (1988).
[18] A. T. J. B. Eppink and D. H. Parker, Rev. Sci. Instrum. **68**, 3477 (1997).
[19] D. H. Parker and A. T. J. B. Eppink, J. Chem. Phys. **107**, 2357 (1997).
[20] G. E. Burch and K. R. Wilson, J. Chem. Phys. **56**, 3626 (1972).
[21] R. N. Zare, Mol. Photochem. **4**, 1 (1972).
[22] S. H. Lee, Y. J. Jung, and K. H. Jung, Chem. Phys. **260**, 143 (2000).
[23] Y. J. Jung, M. S. Park, Y. S. Kim, K. H. Jung, and H. R. Volpp, J. Chem. Phys. **111**, 4005 (1999).